

See discussions, stats, and author profiles for this publication at: <https://www.researchgate.net/publication/262812644>

# Quantitative Nonlinear Optical Assessment of Atherosclerosis Progression in Rabbits

ARTICLE *in* ANALYTICAL CHEMISTRY · JUNE 2014

Impact Factor: 5.64 · DOI: 10.1021/ac5005635 · Source: PubMed

---

READS

43

## 7 AUTHORS, INCLUDING:



[Leila B. Mostaço-Guidolin](#)

University of British Columbia - Vancouver

14 PUBLICATIONS 96 CITATIONS

[SEE PROFILE](#)



[Mark Hewko](#)

National Research Council Canada

61 PUBLICATIONS 598 CITATIONS

[SEE PROFILE](#)



[Arkady Major](#)

University of Manitoba

71 PUBLICATIONS 517 CITATIONS

[SEE PROFILE](#)



[Alex Chun-te Ko](#)

National Research Council Canada

36 PUBLICATIONS 269 CITATIONS

[SEE PROFILE](#)

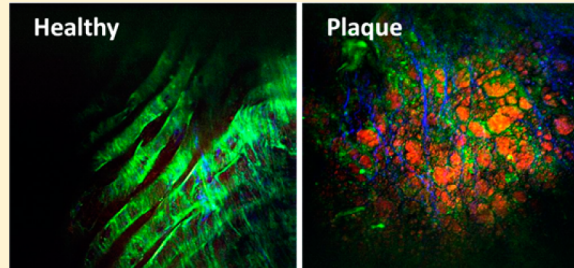
## Quantitative Nonlinear Optical Assessment of Atherosclerosis Progression in Rabbits

Leila B. Mostaço-Guidolin,<sup>†,‡</sup> Elicia K. Kohlenberg,<sup>†</sup> Michael Smith,<sup>†</sup> Mark Hewko,<sup>†</sup> Arkady Major,<sup>‡</sup> Michael G. Sowa,<sup>†</sup> and Alex C.-T. Ko\*,<sup>†,‡</sup>

<sup>†</sup>National Research Council Canada, Medical Devices Portfolio, 435 Ellice Avenue, Winnipeg, MB, Canada R3B 1Y6

<sup>‡</sup>Department of Electrical and Computer Engineering, University of Manitoba, 75A Chancellor's Circle, Winnipeg, MB, Canada R3T 5V6

**ABSTRACT:** Quantification of atherosclerosis has been a challenging task owing to its complex pathology. In this study, we validated a quantitative approach for assessing atherosclerosis progression in a rabbit model using a numerical matrix, optical index for plaque burden, derived directly from the nonlinear optical microscopic images captured on the atherosclerosis-affected blood vessel. A positive correlation between this optical index and the severity of atherosclerotic lesions, represented by the age of the rabbits, was established based on data collected from 21 myocardial infarction-prone Watanabe heritable hyperlipidemic rabbits with age ranging between new-born and 27 months old. The same optical index also accurately identified high-risk locations for atherosclerotic plaque formation along the entire aorta, which was validated by immunohistochemical fluorescence imaging.



Atherosclerosis is a progressive disease. It begins as a fatty streak on the endothelial surface, and gradually develops into a focally thickened intima. Although the etiology of atherosclerosis is not completely understood, historically, atherosclerosis has been regarded as a disease of vascular lipid accumulation with endothelial alterations mainly left out of the picture until recently.

The response-to-injury hypothesis<sup>1,2</sup> postulates that noxious agents, such as shear stress and oxidizing molecules, damage the endothelium, resulting in increased permeability and enhanced expression of cell adhesion molecules. The ensuing infiltration of inflammatory cells starts a complex process of persistent inflammation and vascular remodeling, which stretches over decades and leads to the development and progression of atheromatous plaques, aneurysms, and arterial thrombosis.

Infiltrating leukocytes scavenge lipids and are subsequently transformed to foam cells, making up the bulk of early lesions.<sup>3</sup> The ensuing inflammation attracts more leukocytes and stimulates vascular smooth muscle cells to proliferate and migrate toward the intima.<sup>4</sup> The accumulation of smooth muscle cells is the predominant source of extracellular matrix (ECM) proteins, such as collagen and elastin, which contribute to progressive plaque growth and arterial remodeling.<sup>5,6</sup> In advanced lesions, circumferential stress from high arterial blood pressure has direct impact on the structural integrity of the protective fibrous cap. The fibrous cap of advanced atheromas gradually becomes thinner (and weaker) at the plaque shoulders and ultimately ruptures. As a consequence, the thrombotic content of the necrotic core is exposed to the blood,<sup>7–9</sup> thus leading to thrombus formation which occludes the artery. Resulting blockage of blood flow often causes acute

ischemia in downstream organs, which may result in loss of function and, ultimately, in death. Therefore, having the capability to differentiate high-risk from stable atheroma becomes important in clinical evaluation. Developing new methodologies to identify morphological features of various stages of atherosclerosis development would enable standardization of clinical interpretation of atherosclerotic progression and aid in studying the relationship between plaque morphology, composition, pathophysiology, and clinical repercussions.

Conventional clinical imaging techniques such as X-ray fluorescence angiography,<sup>10</sup> intravascular ultrasound (IVUS),<sup>11–13</sup> and magnetic resonance imaging (MRI)<sup>14</sup> are widely used for detecting and localizing stenotic lesions in patients,<sup>9,11–13</sup> however, they are not sensitive tools for detecting nonstenotic lesions due to low spatial resolution and lack of in vivo chemical specificity. In vivo differentiation of plaque type and assessment of plaque burden still largely rely on the use of IVUS. Although IVUS allows visualization of the geometry of the artery and atherosclerotic lesions,<sup>11–13</sup> according to histopathological studies, it lacks the required specificity and sensitivity in detecting early lesions and lipid-rich lesions.

Recently, optical coherence tomography (OCT) demonstrated strong clinical potential in anatomical imaging for atherosclerosis.<sup>15–18</sup> Despite its high-resolution visualization of vessel wall structures, OCT does not provide chemical

Received: February 10, 2014

Accepted: June 3, 2014

Published: June 3, 2014

identification of plaques. Exogenous labeling or a secondary modality with higher biochemical specificity is required for confirmation. For example, in a very recent study, Liang et al.<sup>19</sup> reported an intravascular optical imaging system with integrated fluorescence and OCT functionalities, demonstrated through excised arterial tissue of normal rabbit injected with model plaque material of highly saturated grease. The plaque material could only be confirmed as high-lipid material by fluorescence imaging after labeling with Annexin V-conjugated Cy 5.5.

Another emerging optical technique, nonlinear optical imaging microscopy (NLOM), has also demonstrated its utility in imaging vascular structures, including atherosclerotic lesions. Multimodal NLOM imaging is capable of rapidly surveying bulk arterial tissue and providing information related to the key biochemical components and structures that portend advanced atherosclerosis. One of the best attributes of NLOM for tissue imaging is that it can be operated without labeling. These label-free NLOM contrasts can be attributed to its intrinsic sensitivity toward specific structural proteins and lipid-rich structures.<sup>20–24</sup> Extensive studies have confirmed that major extracellular components such as elastin and collagen gave rise to strong two-photon excited fluorescence (TPEF) and second-harmonic generation (SHG) signals, respectively.<sup>25–27</sup> Although extracellular collagen also exhibits TPEF, it is much less bright; therefore collagen fibril distribution has been mainly investigated with SHG imaging.

The third NLOM modality, coherent anti-Stokes Raman scattering (CARS), was demonstrated highly useful for high-resolution visualization of biological structures with dense, long-chain C–H groups, such as extracellular lipid droplets and intracellular lipids.<sup>28–30</sup> Using two colinear wavelengths, the pump and the Stokes beams, CARS is capable of selective imaging of lipids and lipid-rich extracellular structures when the energy difference between the pump and the Stokes is tuned to match the signature CH<sub>2</sub> stretching vibrations at ~2845 cm<sup>-1</sup>.

In arterial imaging, each of these NLOM methods has been used to capture the biochemical morphology of major biomolecules accumulated on the arterial wall, for example TPEF for extracellular elastin structures, SHG for type-1 collagen fibrils, while CARS for depositions of lipid-laden extracellular structures. While elastin and collagen are major structural proteins implicated in the remodeling of the arterial wall during plaque development, lipid accumulation is a hallmark feature of atherosclerosis. Atherosclerosis imaging has been reported using various forms of NLOM,<sup>31–38</sup> and a number of studies have compared histoimmunochemical sections of atherosclerotic tissues with corresponding NLOM images of adjacent sections for confirmation.<sup>35,39–41</sup> These studies clearly indicated strong correlation between NLOM signatures and the extracellular changes in tunica media and internal elastic lamina (IEL) during atherosclerosis progression.

In order for NLOM to translate into a clinical imaging tool, not only does it need to provide reliable chemical data but also needs to be compatible with catheterization. Angioscopy is a common imaging tool in clinical assessment of atherosclerosis. As a conventional imaging-based endoscopic technique, it provides almost no biochemical contrast. Adding biochemical specificity through integration of a secondary imaging modality within a medical catheter is an attractive approach to improve the sensitivity and specificity of conventional endoscopic imaging. The concept of NLO endoscope has been around for many years, yet it faces several technical challenges.

Recently, several studies have started to demonstrate significant progress toward overcoming these technical barriers, which have earlier prevented realization of a clinical NLO endoscope.<sup>42–44</sup> These challenges include, but are not limited to, inefficient transmission of ultrafast laser pulses in fiber optics and miniaturization of optical scanning mechanism at the fiber tip. Prototypes and patent applications have been published recently, demonstrating the feasibility and clinical potential of a NLO endoscope in the near future.

While the technology has evolved from a benchtop tool to a potential clinical device, very few studies have in fact investigated the potential of quantitative NLOM imaging in correlating with atherosclerosis progression, which we believe is a very important step to bridge the gap between technological development and actual clinical acceptance.

Previously, we have reported a preliminary study of a quantitative NLOM method for tracking atherosclerosis plaque burden using NLOM data collected from four rabbits of various ages.<sup>38</sup> The current study expanded on this basis and included a much larger and more complete sample size in order to evaluate the true correlation between these newly proposed quantitative NLOM data metrics and the expected temporal pattern of plaque accumulation within the aorta of these rabbits.<sup>45</sup>

Moreover, in this study we also explored the possibility of using the proposed NLOM image metrics to identify high-risk locations of atherosclerosis development along the aorta. It was found that atherosclerotic lesions show a remarkably consistent distribution pattern throughout the arterial lumen, being mostly confined to branch points of large- and middle-sized arteries.<sup>46</sup> Typical sites of atherosclerotic burden include the carotid bifurcation, aortic arch, coronary arteries, the aorta near branch points of intercostal, renal, and mesenteric arteries, as well as the iliac bifurcation. These sites correspond to deviant hemodynamic blood flow conditions compared to the laminar flow pattern that is found in the greater part of the vasculature.<sup>47</sup> Complementary immunohistochemistry tests based on the expression of intercellular adhesion molecules (ICAM) were also performed to confirm these critical locations along the aorta.<sup>48</sup> ICAM fluorescence imaging results were compared with data processed using the proposed quantitative NLOM image metrics. The results of this work demonstrate that the developed quantitative analysis of NLOM images can be used to greatly enhance the quality and reliability of clinical interpretation of atherosclerosis progression.

## EXPERIMENTAL SECTION

All animal experiments conformed to the guidelines set out by the Canadian Council on Animal Care regarding the care and use of experimental animals and were approved by the local Animal Care Committee of the National Research Council of Canada.

**Animal Model and Tissue Preparation.** A rabbit model developed for studying atherosclerosis was used for this study. The myocardial infarction prone Watanabe heritable hyperlipidemic (WHHL-MI) rabbits spontaneously develop atherosclerotic plaques without modified diet due to a hereditary defect in low-density lipoprotein (LDL) processing.<sup>49,50</sup> Arterial tissues were harvested from a total of 21 WHHL-MI rabbits that were sacrificed at ages ranging from new born to 27 months. This sampling represents stages of atherosclerotic disease progression, with the 27 month-old rabbit considered to be at the end of its natural life cycle based on the observation

that both the 24- and the 27-month-old rabbits died of natural causes. A schematic illustration of the adopted procedure is shown in Figure 1.

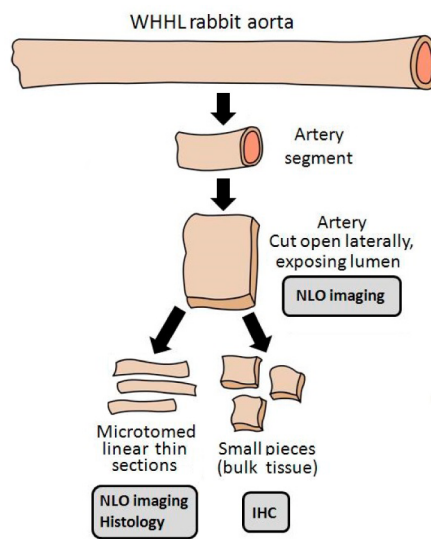


**Figure 1.** Overview/schematic of sample cutting adopted in this study. The aorta was divided into four segments; each segment was further divided into smaller pieces to be used for NLOM imaging, histology, and immunohistochemistry validation experiments.

The excised aorta was dissected from the ascending aorta to the external iliac artery and then rinsed in heparinized saline. The exterior surfaces of the harvested aorta tissue were delicately cleaned of connective tissue prior to subdividing the aorta into four tissue segments. Each of these segments represents a specific location along the artery, as illustrated in Figure 2: the aortic arch (AA), thoracic artery (TA), abdominal artery (AbA), and external iliac artery (EIA).

These bulk artery samples were placed on a moist surface in Petri dishes with the luminal surface facing up. Hydration was maintained throughout the measurements by periodic application of PBS solution on the luminal surface. Digital photographs of the luminal surface were acquired and regions of interest were identified prior to imaging. More procedural details can be found elsewhere.<sup>35,38</sup> After imaging, a portion of

each piece of bulk tissue was set aside for histology and immunohistochemistry.

**Histology.** The artery was cross-sectioned on a cryotome into 8  $\mu\text{m}$  thin sections while embedded in optical cutting temperature medium. The tissue sections were immersion-fixed in either 95% ethanol or 10% buffered formalin based on individual staining protocols. Three different types of staining were carried out. Hematoxylin and eosin (H&E) staining revealed general tissue morphology, picro-sirius red highlighted collagen/elastin fibers under circularly polarized condition, and oil red O staining accented high-lipid structures. Unlabeled artery sections imaged under the NLOM microscope were then compared to adjacent stained sections for validation. Histological images were obtained using a 10 $\times$  air objective lens on a Zeiss Axio Observer Z1 system equipped with AxioCam ICC3 CCD camera (Carl Zeiss Canada, Toronto, ON, Canada).

#### Immunohistochemistry and Fluorescence Imaging.

Bulk tissue immunohistochemistry tests based on near-IR fluorescence imaging of intercellular adhesion molecule 1 (ICAM-1) was carried out in order to confirm and quantify the plaque severity at various locations along the aorta. Binding and recruitment of circulating leukocytes to the vascular endothelium and further migration into the subendothelial spaces are major processes in the development of atherosclerosis and are mediated through a diverse family of cellular adhesion molecules that are expressed on the surface of vascular endothelial cells.<sup>51</sup> Among all identified adhesion molecules, the expression and biological properties of intercellular adhesion molecule 1 (ICAM-1) are well-characterized.<sup>52–54</sup> ICAM-1 concentration is elevated during inflammatory conditions in which detailed pathology studies have documented increased expression of cellular adhesion molecules on endothelial cells and other tissue types.<sup>55–57</sup> Frozen arterial tissue samples from 6 rabbits representing different age groups were cut into smaller segments and then fixed for 10 min at room temperature in methanol (MeOH). Samples were then washed three times with phosphate-buffered saline (PBS) followed by incubation in a 10% normal goat serum solution (in PBS with 0.03% Triton) at room temperature for 1 h and then washed once with PBS. Samples were then incubated overnight with 1:250 solution of Cy5.5-labeled mdAb-ICAM. Samples were washed once with PBS and kept in PBS until imaging. After imaging, samples were stored in the –80 °C

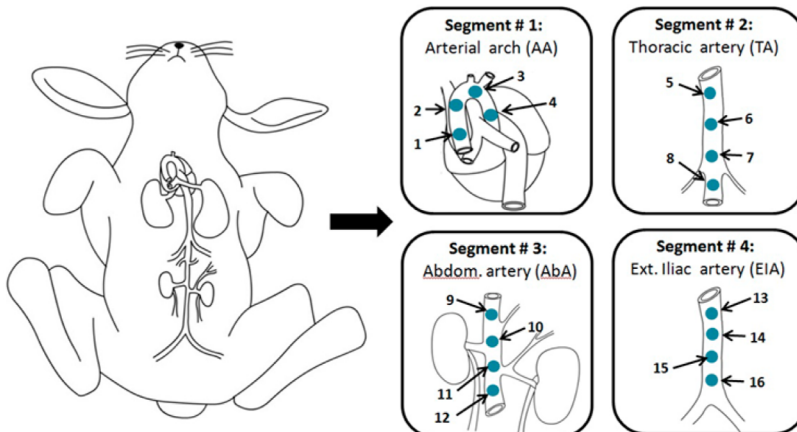


**Figure 2.** Points along the aorta which were used as a reference for NLOM measurements. These points represent locations of interest to be studied with respect to plaque burden along the blood vessels.

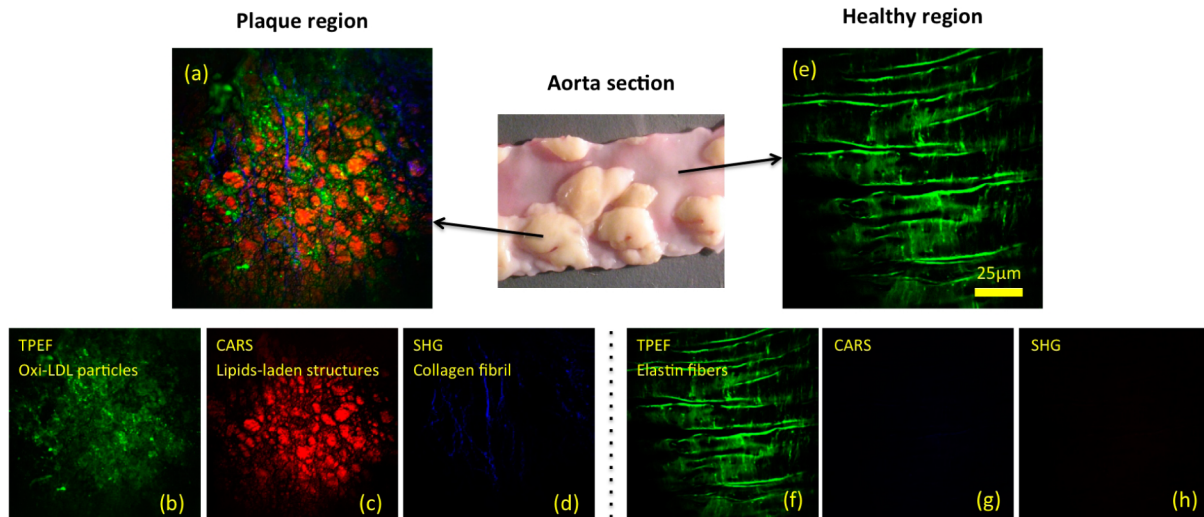


**Figure 3.** Representative epi-NLOM images of a WHHL-MI rabbit's artery wall, acquired from (a) plaque surface and (e) healthy artery wall. Images (b–d) and (f–h) are premerged TPEF, SHG, and CARS images for (a) and (e), respectively.

freezer. The Cy5.5 dye present in mdAb-ICAM was stimulated with an array of light-emitting diodes emitting at 675 nm. The fluorescence was obtained at 700 nm, and the images were acquired using a Photometrics CCD camera at a 1 s acquisition time, defined after testing the signal-to-noise ratio for each sample. The CCD camera was equipped with a 700 nm cut-off filter. All of the fluorescence data collected were analyzed using Matlab. The region containing the sample in each image was segmented, in order to consider only the pixels which were carrying information regarding the sample itself; in other words, the background area where no sample was present was not counted. The mean fluorescent intensity for each image was computed by averaging over all pixels carrying the sample's fluorescence information.

**CARS-Based Multimodal Nonlinear Optical Microscopy.** A custom-built multimodal nonlinear optical (NLO) laser scanning microscope was used for two-photon-excited fluorescence (TPEF), second harmonic generation (SHG), and coherent anti-Stokes Raman scattering (CARS) imaging of arterial tissue. For bulk tissue samples, all signals were collected in the epi-direction. Technical details of the NLO microscope were previously reported.<sup>35</sup> In summary, this is a NLO microscope powered by a femtosecond Ti:sapphire oscillator (Tsunami, Spectra-Physics). The Ti:sapphire oscillator was pumped by 8 W of green laser light at 532 nm (Mellellium Pro, Spectra-Physics) and produced 100 fs pulses centered at 800 nm. The pulse train was divided into two beams; one beam was used to generate tissue TPEF and SHG signals, and the other beam was coupled into a photonic crystal fiber (PCF) to generate a supercontinuum (SC). In this arrangement, the CARS signal was generated by spatially and temporally overlapping the pump beam (fs pulses at 800 nm) and the Stokes beam (the near-IR portion of the SC emission from the PCF, which was selected by using a bandpass filter). The frequency difference between the pump and the Stokes beams was tuned to match the vibrational frequency of the C–H stretching mode for fast lipid imaging. This system was equipped with three nondescanned PMT detectors for capturing colocalized TPEF, SHG, and CARS signals simultaneously through an array of optical filters and dichroic mirrors. A 20 $\times$ , 0.75 NA air objective lens (Olympus) was used

for both laser focusing and epi-imaging in order to maintain a reasonably sized field of view and good spatial resolution. During imaging, typical laser powers measured at the sample were 25 mW for the pump beam and 8 mW for the Stokes beam. Scanimate software (version 3.5) was used for controlling hardware and acquiring images.<sup>58</sup> Corrections for illumination variations, dark current, and signal intensity normalization were performed according to the procedures outlined previously.<sup>59</sup>

## RESULTS AND DISCUSSION

### Indexing Atherosclerosis Progression with NLOM Image Parameters.

In Figure 3, representative biomorphological features of atherosclerotic arterial lumen (Figure 3a) and healthy artery wall (Figure 3e) were visualized utilizing multimodal NLOM imaging. Covered with complex extracellular components, the surface of an atherosclerotic plaque (shown in Figure 3a) revealed abundant lipid-laden structures and the formation of thick collagen fibrils. No significant contribution from elastin proteins was observed. The bright green particles shown in the TPEF image are likely to be oxidized low-density lipoproteins (ox-LDL). In contrast, a healthy arterial wall showed intact internal elastic lamina (mainly elastin) with no lipids. A small amount of collagen was also observed as part of the intrinsic tunica intima structure.<sup>60</sup>

Premerged TPEF, SHG, and CARS images for Figure 3 (panels a and e) are illustrated in Figure 3 (panels b–d and f–h), respectively.

Certain types of biomorphological changes can be tracked by each of the nonlinear signals (e.g., collagen by SHG and lipids by CARS).

None of these signals by itself, however, was able to provide a reliable correlation between NLOM image features and atherosclerosis progression.<sup>32</sup> In order to improve the level of correlation, we previously proposed a new multidimensional approach to tracking atherosclerosis progression with NLOM image characteristics. This approach not only took into account contributions from each individual channel (TPEF, SHG, and CARS) but also included interchannel signal correlations. Our new discriminatory parameter, optical index for plaque burden

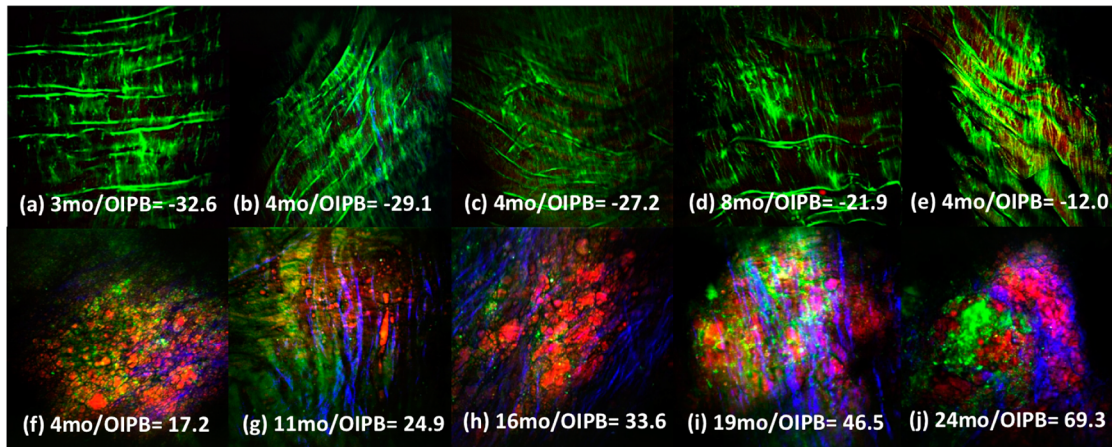


**Figure 4.** (a–e) Representative epi-NLOM images obtained from the (f–j) luminal surface of healthy rabbit aorta obtained from the luminal surface of atherosclerotic plaques. Each image is labeled with the age of the rabbit when it was sacrificed and its corresponding OIPB index calculated using eq 1. Images were collected using a 20 $\times$  air objective lens.

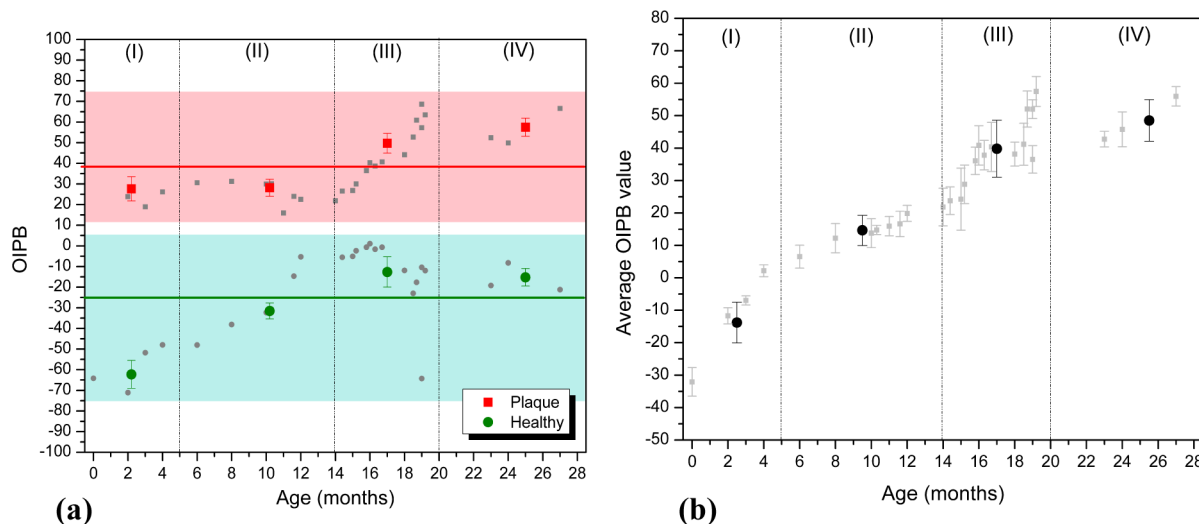


**Figure 5.** (a) Mean OIPB values for images acquired from plaque (large squares) and healthy (large circles) regions of each rabbit, plotted against rabbit's age. Each small point represents data acquired from a single rabbit with indicated age on the chart. The big symbols represent the mean value of each region. As the rabbit's age increases, regions dominated by plaque show higher OIPB values, suggesting that the lesions are advancing with age. The solid line is the mean value, considering all animals, and the two colored regions are the standard deviation around the mean. (b) Mean OIPB values for all rabbits, considering both plaque and healthy regions. Each small point represents data acquired from a single rabbit with indicated age on the chart. The Greek numbers on top of each graph are associated with age groups presenting similar histopathological patterns. (Buja et al.<sup>36</sup>). The solid black circles represent the overall mean OIPB value for each age group.

or OIPB (eq 1), was tested and found to be useful in differentiating the atherosclerotic plaque burden.<sup>38</sup>

The OIPB index is a linear expression of several image statistics extracted from NLO images obtained from the arterial lumen of rabbit aortas. These values are derived primarily from signal intensity and the interchannel intensity correlation between three intrinsic NLO signals (TPEF, SHG, and CARS). Preliminary results obtained from 4 WHHLMi rabbits suggested a semilinear correlation between OIPB index and atherosclerosis progression.<sup>38</sup> The OIPB index can be expressed as

$$\text{OIPB} = \text{SS}_{\text{SHG}} + \text{SS}_{\text{CARS}} + d(\text{SS}_{\text{SHG}}, \text{SS}_{\text{TPEF}}) \\ + d(\text{SS}_{\text{CARS}}, \text{SS}_{\text{TPEF}}) + d(\text{SS}_{\text{CARS}}, \text{SS}_{\text{SHG}}) \quad (1)$$

Equation 1 contains 5 parameters that are extracted from NLOM images. Each  $\text{SS}_x$  term is the ratio of signal to density

( $S/D$ ), where  $S$  (signal) is the average signal value for the image and  $D$  (density) the density of pixels with significant signal divided by the total number of pixels in each image ( $512 \times 512$ , in our case).

Significant signal corresponds to the number of pixels showing signal intensity above a pre-established threshold divided by the total number of pixels ( $512 \times 512$ ) of the acquired image. The threshold is established by computing the average signal level measured from multiple background locations, in the absence of any targeted molecular structures (e.g., collagen fibrils).

The NLO signals are designated by subscript (SHG, CARS, or TPEF).<sup>38,59</sup> The term  $d(\text{SS}_x, \text{SS}_y)$  is the numerical difference between two SS scores, for example,  $d(\text{SS}_{\text{CARS}}, \text{SS}_{\text{TPEF}}) = \text{SS}_{\text{CARS}} - \text{SS}_{\text{TPEF}}$ . Note that the  $\text{SS}_{\text{TPEF}}$  score was not included on its own in the calculation of OIPB because it provided no additional contrast for discrimination between

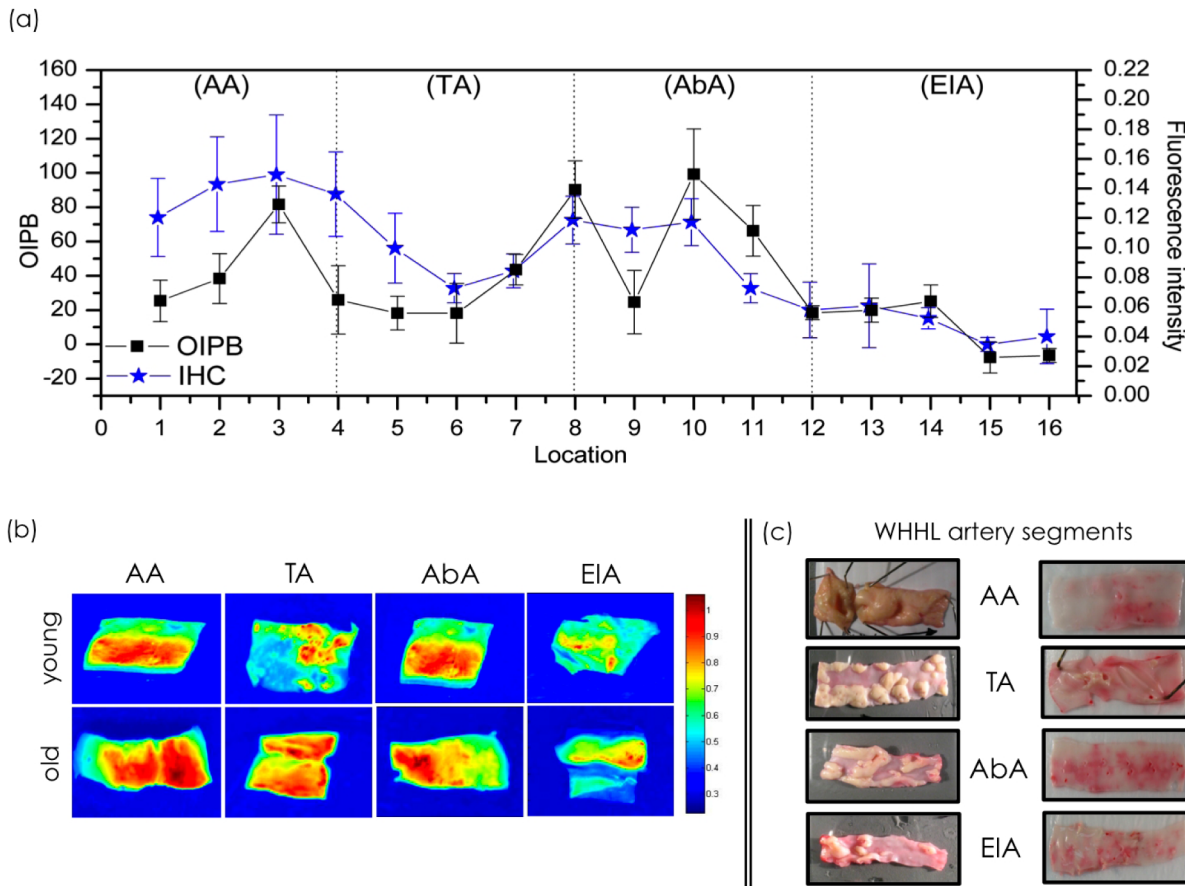


**Figure 6.** (a) OIPB values and immunohistochemistry (IHC) data obtained for each point along the aorta; (b) average fluorescence intensity values related to ICAM-1 distribution in arterial samples from WHHL rabbits. In both cases, the highest values can be associated with severe plaque accumulation. Those values were obtained mainly at branch and vessel bifurcations, confirming the capability of this index to also track/highlight the plaque burden along the aorta. The correlation coefficient obtained when comparing the OIPB and IHC values is 0.6. AA, aortic arch; TA, toracic artery; AbA, abdominal aorta; and EIA, external iliac aorta.

atherosclerosis lesions from the healthy vessel wall based on preliminary data. Detailed discussion of the selection and interpretation of each term in eq 1 can be found elsewhere.<sup>38</sup>

The OIPB index is a tool developed to quantify atherosclerotic plaque development as a function of the variations of four main extracellular components represented in multimodal NLO images: collagen, lipid deposition, elastin fibers, and other fluorescent macromolecules. Examples of OIPB indices and images are illustrated in Figure 4. Each image in Figure 4 is shown with its corresponding OIPB index (highlighted in yellow). Figure 4 (panels a–e) show relatively healthy lumen with low OIPB indices, while Figure 4 (panels f–j) show representative images of atherosclerotic lumen captured at increasing ages with correspondingly higher OIPB indices. Figure 4f shows an image of a plaque from a 4-month-old rabbit artery which has an OIPB of 17.3, whereas Figure 4j, shows an image of a 24-month-old rabbit artery, which has an OIPB value of 69.3.

The average OIPB indices obtained from images of healthy lumen surfaces ( $OIPB_{\text{healthy}}$ ) and atherosclerotic ( $OIPB_{\text{athero}}$ ) locations are plotted against rabbit's age in Figure 5a. Each point shown in this plot corresponds to the mean OIPB value obtained from regions either dominated by plaque or free of plaques. The horizontal coordinate represents the age of each rabbit when it was sacrificed. In the majority of these 21 rabbits, the values of  $OIPB_{\text{athero}}$  are significantly higher than those of

$OIPB_{\text{healthy}}$ . The  $OIPB_{\text{healthy}}$  values are distributed between –73 and 5, while most  $OIPB_{\text{athero}}$  values range from 15 to 70. The high level of  $OIPB_{\text{athero}}$  values are attributed to the higher level of collagen remodeling and higher-density of lipid deposition in plaques, thus translating into the higher  $SS_{\text{SHG}}$  and  $SS_{\text{CARS}}$  terms.

Other information, such as unique patterns of lesion development are also noticed. In Figure 5a, it shows that  $OIPB_{\text{healthy}}$  index increases steadily over the first 14–15 months period (shaded in green) before leveling off, whereas the  $OIPB_{\text{athero}}$  index is relatively stable before the 14–15 months period and then jumps up very quickly reaching a new high. This observation suggests that in this rabbit model, there seems to be a critical time window when atherosclerotic plaques undergo the most prominent lipid and collagen deposition, which can be associated with the disease progression. In our case, this time window is between 15 and 20 months of the rabbits' life cycle. Although no direct histological evidence has been reported to date for such a pattern of atherosclerosis progression, this observation has the potential to greatly impact therapeutic strategies if it can be proved to be true histologically in the future.

In Figure 5b, the mean OIPB values from all rabbits are presented as a function of age. In this plot, each rabbit was represented by a mean OIPB value, obtained by averaging data collected from all imaged healthy lumen and atherosclerotic

locations. The index shows a clear correlation with age. Since plaque burden increases with the age of the rabbit in this model,<sup>45</sup> this result implies that the OIPB value is quantitatively indicative of the severity of the atherosclerotic lesions or plaque burden. The groups (I), (II), (III), and (IV) indicated in Figure 5 (panels a and b) represent age groups which present similar histopathological patterns in the arterial wall, according to a previous study reported by Buja et al.<sup>45</sup> Group (I) contains data from rabbits aged from 0 to 5 months; group (II) presents data collected from 5.5 to 14 months old animals; and group (III) and (IV) show data acquired from the rabbits within the 14.5 to 20 months and 20.5 to 27 months aged groups, respectively.

Previously, Kolodgie et al.<sup>60</sup> published an extensive report tracking the progression and the varying levels of atherosclerotic plaques in WHHL rabbits, using histology and SEM imaging. Kolodgie's study indicated that the degree of atherosclerotic progression correlated closely with rabbit's age and animals older than 12–14 month-old showed signs of severe atherosclerosis. These conclusions are consistent with observations revealed by the OIPB data. Another point to be made for Figure 5b is that, statistically speaking, the difference between the OIPB values of age groups (II) and (III) is significant. In contrast, the OIPB values of age groups (III) and (IV) are not statistically different, suggesting that after a critical age (e.g., 18–20 month-old), the disease has already reached its most severe stage. As the OIPB is very sensitive tracking the accumulation of lipid-rich cells and collagen, we can build the hypothesis that this index has a great potential tracking the disease progression.

**Indexing Plaque Burden at Critical Locations along the Aorta.** During the course of atherosclerosis progression, certain locations along the aorta are more prone to plaque development than others.<sup>36,61–62</sup> These locations include transition zones such as bends, arches, and bifurcations. At these locations, the rate and pattern of blood flow are altered thus affecting local hemodynamics.<sup>63–65</sup>

Attempts have been made to assess the role of hemodynamic factors in atherosclerosis by correlating the distribution of intimal lesions, usually in excised collapsed arteries, with presumed changes in blood flow conditions or with flow patterns visualized in idealized glass or plastic models. Elevations or variations in flow velocity and shear stress,<sup>66,67</sup> flow separation,<sup>68</sup> and turbulence<sup>69–71</sup> have each been proposed as hemodynamic potentiator of lesion formation.

The relation between vessel wall shear stress and the development and progression of atherosclerosis has been well-established.<sup>70–72</sup> Low and oscillating wall shear stress seems to favor the development of atherosclerosis as determined by the inverse relation between the wall shear stress and arterial wall thickness.<sup>73–75</sup> Wall shear stress also seems to depend on age, blood pressure, and body mass index. The value of wall shear stress is subject-specific and vessel-specific. Wall shear stress varies along the same vessel and around the vessel's circumference.

In this context, since we have demonstrated that OIPB index was a good indicator for assessing plaque burden in a longitudinal study, it would be interesting to test if OIPB index is also capable of accurately detecting higher plaque burden at critical locations along the aorta. NLOM images acquired at four predefined points per segment (i.e., arterial arch, thoracic artery, abdominal artery, and external iliac artery) were thus analyzed and then compared with immunohisto-

logical data based upon ICAM-1 fluorescence imaging. The approximate location of each point is shown in Figure 2.

The average OIPB value for each point shown in Figure 2, calculated by considering both healthy and plaque regions, is presented in Figure 6a (black trace, with squared points). Note that locations 3, 8, and 10 are characterized by the highest OIPB values, hence the highest plaque burden along the entire aorta tree. When compared with the OIPB data, data from immunohistochemistry (IHC, blue trace) based on ICAM-1 fluorescence intensity showed marked similarity with a calculated correlation coefficient ( $\rho$ ) of 0.6. In addition, Figure 6 (panels b and c) illustrate representative ICAM-1 fluorescence images and white-light video images of the four predefined arterial segments.

Matching results in Figure 6a with location maps in Figure 2, it becomes clear that the 3 locations with the highest OIPB values and ICAM-1 fluorescence intensities correspond to the aortic arch and regions close to the two kidneys' artery branches, respectively.

In the aortic arch, the pattern of blood flow is more complex than in the other regions along the descending abdominal aorta, with constant helical and extensive reversal flow resulting from the curvature of the arch and the strong pulsatility of flow.<sup>70,71</sup> As a result, this turbulence of blood flow and change in arterial wall shear stress leads to an elevated probability of plaque development within the aortic arch.<sup>76</sup> Similarly, regions which are close to artery branches to the kidney also experience nonlaminar blood flow due to arterial bifurcation. This too, significantly enhances the early development of atherosclerosis lesions.<sup>77</sup>

Although similar patterns were observed, the ICAM-1 data does look slightly different from the OIPB data. From Figure 6a, one can see that the drop and rise in OIPB values around these critical locations are much steeper than those presented in the ICAM-1 fluorescence data. This can be explained by the different sampling size of these two very different optical techniques. While each NLOM imaged area is  $200 \times 200 \mu\text{m}^2$  in size (with a 20× objective lens), ICAM-1 fluorescence is typically evaluated over an area of  $\sim 1 \times 1 \text{ cm}^2$ . The smaller sampling size in NLOM gives a more localized snapshot, whereas the ICAM-1 data presents a picture with information averaged over a larger area. This characteristic of NLOM makes it a more sensitive tool in detecting local changes thus generating a sharper contrast between different locations. Nonetheless, regions with a greater tendency to be affected by atherosclerotic lesions were successfully tracked by the OIPB.

Another interesting observation is that as the rabbit's age increases, all four studied aorta regions (AA, TA, AbA, and EIA) show increasing OIPB values. The accumulation of lipid-rich cells and collagen, as previously presented<sup>78</sup> and discussed in this work, suggest that the lesions are advancing with age. On the basis of this evidence, we believe that the OIPB can be a useful tool to optically track the lesions progression.

## CONCLUSIONS

In this study, we presented an intensity-based NLOM image parameter, the optical index for plaque burden (OIPB), and applied it to assessing atherosclerotic plaque burden. On the basis of data collected from 21 WHHL-MI rabbits, we have demonstrated a strong correlation between the OIPB and the severity of atherosclerotic lesions, which increase with the rabbits' age. The OIPB index was also used to accurately identify high-risk locations for plaque formation along the

entire aorta. Identified locations were later validated by immunohistochemical fluorescence imaging. While the OIPP index seems to be an adequate objective indicator of atherosclerosis plaque burden, other relevant NLOM quantitative matrices might be added to improve the quality of clinical interpretation. For instance, including quantitative analysis of collagen fibril orientation from the SHG images<sup>66</sup> and the shape and size of lipid-rich structures from the CARS images might greatly enhance the reliability of this model for objective quantification of plaque burden. Ultimately, this would allow classification of lesions according to the guidelines provided by the American Heart Association using only the NLOM imaging data.

## AUTHOR INFORMATION

### Corresponding Author

\*E-mail: alex.ko@nrc-cnrc.gc.ca.

### Author Contributions

L.B.M.-G. conceived the method, performed imaging measurements, and data analyses. A.C.-T.K. designed the experiments, performed imaging measurements, and supervised the project. M.H. established the rabbit colony, also coordinated animal service and imaging works. M.S.D.S. provided expertise on setting up and maintaining the NLO imaging microscope. A.M. cosupervised the project and also provided assistance in imaging protocols. M.G.S. provided guidance on the image analysis. L.B.M.-G. and A.C.-T.K. cowrote the manuscript with inputs from all other authors.

### Notes

The authors declare no competing financial interest.

## ACKNOWLEDGMENTS

This work is partially supported by the National Research Council Canada, Genomics and Health initiative and Natural Science and Engineering Research Council (NSERC) Discovery Grant in the form of student financial support. We thank Dr. Elda Hegmann (Kent State University, Kent, OH) for all support provided related to the IHC experiments. L.B.M.-G. also acknowledges financial support from Edward R. Toporeck Graduate Fellowship, Berdie Irvin Cohen Fellowship, Elizabeth Anne Hogan Memorial Scholarship, and International Graduate Student Scholarship at University of Manitoba.

## REFERENCES

- (1) Virchow, R. *Thrombosis and Emboli*; Science History Publications: Sagamore Beach, MA, 1998.
- (2) Ross, R.; Glomset, J.; Harker, L. *Am. J. Pathol.* **1977**, *86*, 675.
- (3) Stary, H.; Chandler, A.; Glagov, S.; Guyton, J.; Insull, W., Jr.; Rosenfeld, M.; Scherer, S.; Schwartz, C.; Wagner, W.; Wissler, R. *Arterioscler., Thromb., Vasc. Biol.* **1994**, *14*, 840.
- (4) Raines, E.; Ross, R. *Br. Heart J.* **1993**, *69*, 30.
- (5) Andreeva, E.; Pugach, I.; Orekhov, A. *Atherosclerosis* **1997**, *130*, 133–142.
- (6) MacLeod, D.; Strauss, B.; de Jong, M.; Escaner, J.; Umans, V.; van Suylen, R.; Verkerk, A.; de Feyter, P.; Serruys, P. *J. Am. Coll. Cardiol.* **1994**, *23*, 59–65.
- (7) Stary, H.; Chandler, A.; Dinsmore, R.; Fuster, V.; Glagov, S.; Insull, W., Jr.; Rosenfeld, M.; Schwartz, C.; Wagner, W.; Wissler, R. *Circulation* **1995**, *92*, 1355.
- (8) Kolodgie, F.; Burke, A.; Farb, A.; Gold, H.; Yuan, J.; Narula, J.; Finn, A.; Virmani, R. *Curr. Opin. Cardiol.* **2001**, *16*, 285.
- (9) Libby, P. *J. Int. Med.* **2000**, *247*, 349–358.
- (10) Courtney, B. K.; Munce, N. R.; Anderson, K. J.; Thind, A. S.; Leung, G.; Radau, P. E.; Foster, F. S.; Vitkin, I. A.; Schwartz, R. S.; Dick, A. J.; Wright, G. A.; Strauss, B. H. *Eur. Heart J.* **2008**, *29*, 583–593.
- (11) Sun, J.; Zhang, Z.; Lu, B.; Yu, W.; Yang, Y.; Zhou, Y.; Wang, Y.; Fan, Z. *Am. J. Roentgenol.* **2008**, *190*, 748–754.
- (12) Yock, P. G.; Fitzgerald, P. J. *Am. J. Cardiol.* **1998**, *81*, 27E–32E.
- (13) Hodgson, J. M.; Reddy, K. G.; Suneja, R. *J. Am. Coll. Cardiol.* **1993**, *21*, 35–44.
- (14) Honda, Y.; Fitzgerald, P. J. *Circulation* **2008**, *117*, 2024–2037.
- (15) Barlis, P.; Schmitt, J. M. *EuroIntervention* **2009**, *4*, 529–534.
- (16) Barlis, P.; Serruys, P. W.; Devries, A.; Regar, E. *Eur. Heart J.* **2008**, *29*, 2023.
- (17) Barlis, P.; Ferrante, G.; Del Furia, F.; Di Mario, C. *Med. J. Aust.* **2008**, *188*, 728.
- (18) Jang, I. K.; Tearney, G. J.; MacNeil, B.; Takano, M.; Moselewski, F.; Iftima, N.; Shishkov, M.; Houser, S.; Aretz, H. T.; Halpern, E. F. *Circulation* **2005**, *111*, 1551–1555.
- (19) Liang, S.; Saidi, A.; Jing, J.; Liu, G.; Li, J.; Zhang, J.; Sun, C.; Narula, J.; Chen, Z. *J. Biomed. Opt.* **2012**, *17*, 070501.
- (20) Mertz, J. *Curr. Opin. Neurobiol.* **2004**, *14*, 610–616.
- (21) Yue, S.; Slipchenko, M.; Cheng, J. *Laser Photonics Rev.* **2011**.
- (22) Williams, R.; Zipfel, W.; Webb, W. *Curr. Opin. Chem. Biol.* **2001**, *5*, 603–608.
- (23) Zipfel, W.; Williams, R.; Webb, W. *Nat. Biotechnol.* **2003**, *21*, 1369–1377.
- (24) Evans, C.; Xie, X. *Annu. Rev. Anal. Chem.* **2008**, *1*, 883–909.
- (25) Helmchen, F.; Denk, W. *c. Nat. Methods* **2005**, *2*, 932–940.
- (26) Zoumi, A.; et al. *Biophys. J.* **2004**, *87*, 2778–2786.
- (27) Zipfel, W. R.; et al. *Proc. Natl. Acad. Sci. U.S.A.* **2003**, *100*, 7075–7080.
- (28) Cheng, J.-X.; Xie, X. S. *J. Phys. Chem. B* **2004**, *108*, 827–840.
- (29) Evans, C. L.; et al. *Proc. Natl. Acad. Sci. U.S.A.* **2005**, *102*, 16807–16812.
- (30) Evans, C. L.; Xie, X. S. *Annu. Rev. Anal. Chem.* **2008**, *1*, 883–909.
- (31) Le, T.; Langohr, I.; Locker, M.; Sturek, M.; Cheng, J. *J. Biomed. Opt.* **2007**, *12*, 054007.
- (32) Zoumi, A.; Lu, X.; Kassab, G.; Tromberg, B. *Biophys. J.* **2004**, *87*, 2778–2786.
- (33) Wang, H.; Langohr, I.; Sturek, M.; Cheng, J. *Arterioscler., Thromb., Vasc. Biol.* **2009**, *29*, 1342.
- (34) Wang, H.; Le, T.; Cheng, J. *Opt. Commun.* **2008**, *281*, 1813–1822.
- (35) Ko, A.; Ridsdale, A.; Smith, M.; Mostaco-Guidolin, L.; Hewko, M.; Pegoraro, A.; Kohlenberg, E.; Schattka, B.; Shiomi, M.; Stolow, A.; et al. *J. Biomed. Opt.* **2010**, *15*, 020501.
- (36) Megens, R.; oude Egbrink, M.; Merkx, M.; Slaaf, D.; van Zandvoort, M. *Vital Imaging of Large Arteries using Two-Photon Laser Scanning Microscopy: Focus on the Arterial Wall*; Maastricht University Press, 2008; 87.
- (37) Doras, C.; Taupier, G.; Barsella, A.; Mager, L.; Boeglin, A.; Bulou, H.; Bousquet, P.; Dorkenoo, K. *Opt. Exp.* **2011**, *19*, 15062–15068.
- (38) Mostaco-Guidolin, L.; Sowa, M.; Ridsdale, A.; Pegoraro, A.; Smith, M.; Hewko, M.; Kohlenberg, E.; Schattka, B.; Shiomi, M.; Stolow, A.; et al. *Biom. Opt. Exp.* **2010**, *1*, 59–73.
- (39) Wang, H.-W.; Thuc, T. L.; Cheng, X. *Opt. Commun.* **2008**, *281*, 1813–1822.
- (40) Wang, H.-W.; et al. *Arterioscler., Thromb., Vasc. Biol.* **2009**, *29*, 1342–1348.
- (41) Le, T. T.; et al. *J. Biomed. Opt.* **2007**, *12*, 054007–054007.
- (42) Tu, H.; Boppart, S. *J. Biophotonics* **2014**, 9–22.
- (43) Légaré, F.; Evans, C. L.; Ganikhanov, F.; Xie, S. *Opt. Exp.* **2006**, 4427–4432.
- (44) Smith, B.; Naji, M.; Murugkar, S.; Alarcon, E.; Brideau, C.; Sty, P.; Anis, H. *Opt. Exp.* **2013**, 17161–17171.
- (45) Buja, L.; Kita, T.; Goldstein, J.; Watanabe, Y.; Brown, M. *Arterioscler., Thromb., Vasc. Biol.* **1983**, *3*, 87.
- (46) Caro, C.; Fitz-Gerald, J.; Schroter, R. *Arterial Wall Shear and Distribution of Early Atheroma in Man*; Wiley: New York, 1969.

- (47) Ku, D.; Giddens, D.; Zarins, C.; Glagov, S. *Arterioscler., Thromb., Vasc. Biol.* **1985**, *5* (3), 293–302.
- (48) Walpolo, P.; Gotlieb, A.; Cybulsky, M.; Langille, B. *Arterioscler., Thromb., Vasc. Biol.* **1995**, *15*, 2.
- (49) Shiomi, M.; Ito, T.; Yamada, S.; Kawashima, S.; Fan, J. *Arterioscler., Thromb., Vasc. Biol.* **2003**, *23*, 1239–1244.
- (50) Shiomi, M.; Ito, T.; Yamada, S.; Kawashima, S.; Fan, J. *J. Atheroscler. Thromb.* **2004**, *11*, 184–189.
- (51) Hwang, S. J.; Ballantyne, C. M.; Sharrett, A. R.; Smith, L. C.; Davis, C. E.; Gotto, A. M.; Boerwinkle, E. *Circulation* **1997**, *96*, 4219–4225.
- (52) Davies, M. J.; Gordon, J. L.; Gearing, A. J. H.; Pigott, R.; Woolf, N.; Katz, D.; Kyriakopoulos, A. *J. Pathol.* **1993**, *171*, 223–229.
- (53) Blann, A. D.; Seigneur, M.; Steiner, M.; Miller, J. P.; McCollum, C. N. *Thromb. Haemostasis* **1998**, *79*, 1080–1085.
- (54) Poston, R. N.; Haskard, D. O.; Coucher, J. R.; Gall, N. P.; Johnson-Tidey, R. R. *Am. J. Pathol.* **1992**, *140*, 665.
- (55) Katz, A. M.; Rosenthal, D.; Sauder, D. N. *Int. J. Dermatol.* **1991**, *30*, 153–160.
- (56) Telek, G.; Ducroc, R.; Scoazec, J. Y.; Pasquier, C.; Feldmann, G.; Rozé, C. *J. Surg. Res.* **2001**, *96*, 56–67.
- (57) Albelda, S. M. *Lab. Invest.; a journal of tech. meth. and path.* **1993**, *68*, 4–17.
- (58) Pologruto, T. A.; Sabatini, B. L.; Svoboda, K. *Biomedical Engineering Online* **2003**, *2*, 13.
- (59) Strupler, S.; Pena, A.-M.; Hernest, M. *Opt. Express* **2007**, *15*, 4054–4065.
- (60) Kolodgie, F. D.; Virmani, R.; Rice, H. E.; Mergner, W. J. *Circ. Res.* **1990**, *66*, 1112–1126.
- (61) Di Tullio, M.; Russo, C.; Jin, Z.; Sacco, R.; Mohr, J.; Homma, S. *Circulation* **2009**, *119*, 2376–2382.
- (62) Ku, D. *Annu. Rev. Fluid Mech.* **1997**, *29*, 399–434.
- (63) Shahcheraghi, N.; Dwyer, H.; Cheer, A.; Barakat, A.; Rutaganira, T. *Biomech. Eng.* **2002**, *124*, 378.
- (64) Frangos, S.; Gahtan, V.; Sumpio, B. *Arch. Surg.* **1999**, *134*, 1142.
- (65) Tarbell, J. *Annu. Rev. of Biomed. Eng.* **2003**, *5*, 79–118.
- (66) Fry, D. Hemodynamic Forces in Atherogenesis. In *Cerebrovascular Diseases*; Scheinberg, P., Ed.; Raven Press: New York, 1976, pp 77–95.
- (67) Aoki, T.; Wood, H. A.; Old, L. J.; Boyse, E. A. *Nature* **1969**, *223*, 159.
- (68) Scharfstein, H.; Gutstein, W.; Lewis, L. *Circ. Res.* **1963**, *13*, 580–584.
- (69) Ferguson, G.; Roach, M. *Cardiovascular Fluid Dynamics* **1972**, *2*, 141–157.
- (70) Gutstein, W.; Schneck, D.; Marks, J. *J. Atheroscler. Res.* **1968**, *8*, 381–388.
- (71) Stehbens, W. *Exp. Physiol.* **1959**, *44*, 110.
- (72) Frangos, S.; Gahtan, V.; Sumpio, B. *Arch. Surg.* **1999**, *130*, 1142.
- (73) Tarbell, J. M. *Annu. Rev. of Biom. Eng.* **2003**, *5*, 79–118.
- (74) Gibson, C. Michael; et al. *Arterioscler., Thromb., Vasc. Biol.* **1993**, *13*, 310–315.
- (75) Malek, A. M.; Alper, Seth L.; Izumo, S. *JAMA, J. Am. Med. Assoc.* **1999**, *282*, 2035–2042.
- (76) Cheng, C.; et al. *Circulation* **2003**, *113*, 2744–2753.
- (77) Cecchi, E.; et al. *Atherosclerosis* **2011**, *214*, 249–256.
- (78) Mostaço-Guidolin, L. B.; Ko, A. C. T.; Wang, F.; Xiang, B.; Hewko, M.; Tian, G.; Sowa, M. G. *Sci. Rep.* **2013**, *3*, 10.1038/srep02190.